Rapid Communications

Flexible polarization rotation at the ferroelectric/metal interface as a seed for domain nucleation

Xian-Kui Wei,[1,2,*] Yurong Yang,[3] Leo J. McGilly,[1,4] Ludwig Feigl,[1,5] Rafal E. Dunin-Borkowski,[2] Chun-Lin Jia,[2,6] Laurent Bellaiche,[3,†] and Nava Setter[1,7]

[1]*Ceramics Laboratory, EPFL-Swiss Federal Institute of Technology, CH-1015 Lausanne, Switzerland*

[2]*Ernst Ruska-Centre for Microscopy and Spectroscopy with Electrons and Peter Grünberg Institute, Forschungszentrum Jülich GmbH, 52425 Jülich, Germany*

[3]*Physics Department and Institute for Nanoscience and Engineering, University of Arkansas, Fayetteville, Arkansas 72701, USA*

[4]*Department of Physics, Columbia University, New York, New York 10027, USA*

[5]*Institute for Photon Science and Synchrotron Radiation, KIT - Karlsruhe Institute of Technology, Hermann-von-Helmholtz-Platz 1, 76344 Eggenstein-Leopoldshafen, Germany*

[6]*School of Microelectronics, Xi'an Jiaotong University, Xi'an 710049, China*

[7]*Department of Materials Science and Engineering, Tel-Aviv University, Ramat Aviv 69978, Israel*

(Received 13 October 2017; revised manuscript received 13 June 2018; published 27 July 2018)

The absence of a realistic polarization screening scenario at the pivotal ferroelectric-metal interface impedes the widespread application of low-dimensional ferroelectric heterostructures. Employing quantitative atom-resolved (scanning) transmission electron microscopy and first-principles calculations, we report that structural and chemical reconstruction universally lowers symmetry of the ferroelectric-metal interface. Irrespective of structural and strain mismatch, chemical termination and diffusion, polar catastrophe, and electrode type, the polarization screening is executed by a flexible polarization rotation at several-unit-cell-thick interfaces. By combining nanoscale and atomic-scale microscopy investigations, our *ex situ* electric-field biasing experiments reveal that the monoclinically distorted interfaces may act as seeds to nucleate new domains during the polarization switching process. These findings suggest that the long-standing fatigue issue is expected to be overcome by interface modification engineering at the monolayer scale.

DOI: 10.1103/PhysRevB.98.020102

Ferroelectric materials are promising candidates to serve as commercial memories because of their faster accessing time, lower energy consumption, and potentially lower cost. Recently, the realization of ultrahigh-density ferroelectric nanocapacitor arrays [1,2], at the Tbit in.$^{-2}$ level, makes this aim much closer to a practical application. However, its implementation is impeded by long-standing issues such as fatigue [3–5], retention loss and imprint [6,7] during cyclical switching events. These critical issues affect almost all ferroelectric-based memories, including ferroelectric tunnel junctions [8] and ferroelectric-ferromagnetic heterostructures [9]. A particularly important reason lies in the so-called depolarization field [10], which arises from an incomplete screening of spontaneous polarization (P_S) at ferroelectric-metal interfaces.

Based on precise control of the interface structure [11,12] and first-principles calculations [13–15], more and more studies have pointed out that clarifying the interfacial screening mechanism is the key to resolving the above issues. However, complicated by factors such as structural mismatch, chemical diffusion, and charge discontinuity, first-principles calculations and phenomenological Landau-Ginzburg-Devonshire theory [16] fail to depict a complete screening scenario at unit-cell-scale thick interfaces. This is evidenced by the discrepancy of their screening scenarios from the experimental findings [17–19]. Recently, compensation phenomena have been explored using aberration-corrected scanning transmission electron microscopy (STEM) [20–22]. Nevertheless, imperfections of the imaging mode [23,24], e.g., unavoidable scanning distortion and weak contrast imaging of oxygen, undermine its capability of performing precise structure investigations at such interfaces.

In this Rapid Communication, we investigate the screening mechanism at a variety of ferroelectric/metal interfaces, e.g., $Pb(Zr_{1-x}Ti_x)O_3$ (PZT)/$SrRuO_3$, $BiFeO_3$/$SrRuO_3$, and Au/PZT, using state-of-the-art microscopy characterization techniques. On the basis of quantitative atom-resolved (S)TEM studies [25–27] and first-principles calculations, we report that regardless of structural and strain mismatch, chemical termination, polarization orientation, and polar catastrophe, the polarization screening is executed by monoclinic distortion enabled flexible polarization rotation at the ferroelectric-metal interfaces. *Ex situ* electric-field biasing experiments corroborate that the heterogeneous interfaces are responsible for the nucleation of new domains during the polarization switching process.

Spontaneous polarization (P_S) in perovskite ferroelectrics (ABO_3) is manifested by an overall shift of the polar oxygen octahedral (BO_6) unit with respect to the body center of the A-site cationic frame. Taking tetragonal (T) PZT (space group $P4mm$) as an example, its polarization comprises uniaxial polar displacements between Zr/Ti and Pb atoms

*x.wei@fz-juelich.de
†laurent@uark.edu

 ©2018 American Physical Society

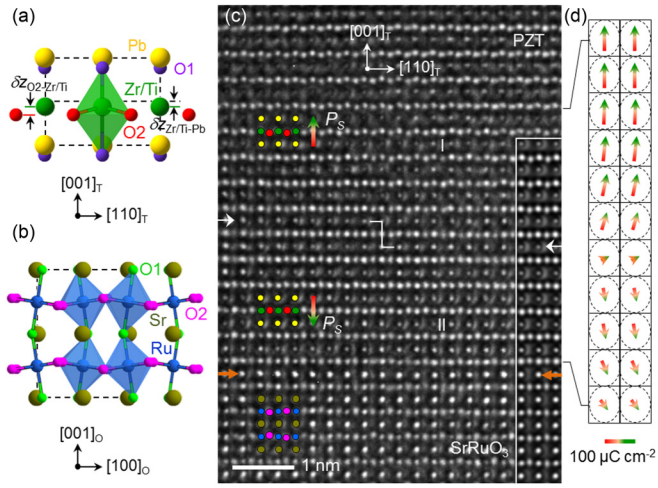

FIG. 1. (a) Crystal structure of tetragonal PZT with an oxygen-octahedral rotation angle $\phi = 0$ viewed along the $[1\bar{1}0]_T$ direction. (b) Crystal structure of orthorhombic $SrRuO_3$ with an oxygen-octahedral rotation angle $\phi \approx 6^\circ$ viewed along the $[100]_O$ direction. (c) Atom-resolved TEM image of $(x = 0.9)\,PZT/SrRuO_3$ interface (constructed upon $DyScO_3$ substrate) along the $[1\bar{1}0]_T \parallel [010]_O$ direction recorded under a negative spherical-aberration imaging (NCSI) condition. The orange arrows mark the SrO-Zr/TiO_2 terminated interface, and the white arrows and polygonal line mark the geometric plane of the CDWs. The inset at the lower right shows a simulated image with a thickness of 5.4 nm and defocus of 6.0 nm. Atomic column types: Pb/O1 (yellow), Zr/Ti (green), O2 (red) in PZT; Sr/O1 (dark yellow), Ru (blue), O2 (pink) in $SrRuO_3$. (d) Local two-dimensional polarization vectors determined from the structure model used for the image simulation.

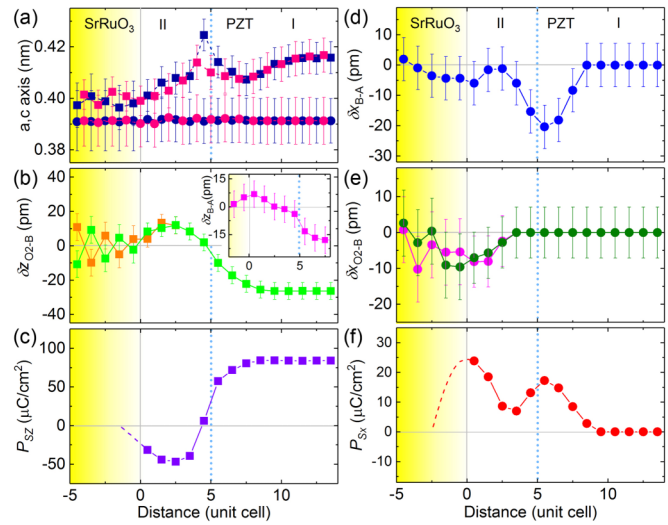

FIG. 2. (a) The c (squares) and a (circles) axes measured from A-site (blue) and B-site (red) atoms, respectively. (b) Out-of-plane displacements of O2 atoms ($\delta z_{O2\text{-}B}$) and (inset) B-site atoms ($\delta z_{B\text{-}A}$). (c) Out-of-plane polarization (P_{SZ}) extrapolated into the $SrRuO_3$ (purple dashed line). (d), (e) In-plane displacements of B-site ($\delta x_{B\text{-}A}$) and O2 ($\delta x_{O2\text{-}B}$) atoms, respectively. (f) In-plane polarization (P_{SX}) extrapolated into the $SrRuO_3$ (red dashed line). These profiles are plotted as a function of distance normal to the interface. The blue dotted lines mark the position of the CDW. The yellow shadow denotes the reduced electron density of $SrRuO_3$ in terms of a decreased rotation of oxygen octahedra towards the interface.

($\delta z_{Zr/Ti\text{-}Pb}$), O2 and Zr/Ti atoms ($\delta z_{O2\text{-}Zr/Ti}$), and O1 and Pb atoms ($\delta z_{O1\text{-}Pb}$) along the $[001]_T$ direction [Fig. 1(a)]. For oxide electrodes, e.g., orthorhombic (O) $SrRuO_3$ (space group $Pbnm$) [Fig. 1(b)], its structure is featured by antiphase and in-phase rotations of the oxygen octahedra along the orthogonal $[101]_O$, $[10\bar{1}]_O$ axes and along the $[010]_O$ axis, i.e., $a^-a^-c^+$ in Glazer's notation [28]. For typical Au and Pt electrodes, both of them have face-centered-cubic structures (space group $Fm\bar{3}m$). At the ferroelectric-metal interfaces, their structures are always complicated by the effects of oxygen-octahedral rotation mismatch, chemical termination and diffusion, polar catastrophe, and so on [11,20,21].

As the PZT film is grown on a $DyScO_3$ substrate, tensile strain (~0.9%) leads to the formation of a ferroelastic $c/a/c/a$ domain array [29] (see Supplemental Material Fig. S1 [30]). In order to unravel the details of these mismatches, $[1\bar{1}0]_T \parallel [010]_O$ oriented $(x = 0.9)\,PZT/SrRuO_3$ specimens are prepared for the TEM study. Figure 1(c) shows an atomically resolved TEM image of a $PZT/SrRuO_3$ interface. As evidenced by the simulated image [the inset in Fig. 1(c)], all atomic columns are clearly resolved, in which the Pb-O1 shows a single column of Pb/O1 due to their small interatomic separation and exhibits a weak contrast at this sample thickness (~5.4 nm). The vertical shifts of the oxygen columns (red circles) in opposite directions with respect to the neighboring Zr/Ti columns (green circles) mark two domains in this image area: domain I, with larger downward shifts of O2, and domain II, with smaller upward shifts. These two domains form a tail-to-tail 180° charged domain wall (CDW) with the wall planes normal to the polarization directions and bridged by a unit-cell step in the middle region. Below domain II, the brighter atom columns well define that the interface is terminated by SrO-Zr/TiO_2 atomic planes. Furthermore, buckling of the O2-Ru-O2 atomic planes clearly displays the in-phase octahedral rotation of $SrRuO_3$ along the $[010]_O$ direction.

In order to unravel the polarization compensation mechanism, an image-simulation-based quantitative TEM study was performed to determine the atomic positions near the interface and the CDW [41]. By removing artifacts affecting the intensity peak positions in the experimental image, e.g., specimen tilting away from the Laue orientation, residual lens aberrations, and the interfacial element diffusion (see Supplemental Material Fig. S2 [30]), measurements of individual atomic shifts with picometer precision become possible.

Figure 2(a) shows the lattice parameter changes as a function of distance normal to the interface. Compared with the nearly constant pseudocubic (p) a_p axis ($a_p = \sqrt{2}a_O/2$ for $SrRuO_3$ and $a_p \approx a_T$ for PZT), ~0.3913 nm, pronounced changes are observed along the c-axis direction. Via a smooth reduction in domain I ($c = 0.4160$ nm, $c/a = 1.063$), the c axis measured from Pb atoms (blue squares) steeply increases to 0.4246 nm ($c/a = 1.085$) near the CDW. A stepwise decrease is then observed in the middle of domain II ($c/a \approx 1.042$) and near the interface ($c/a = 1.025$). The c axes measured from Zr/Ti atoms (pink squares) show smaller values, which diverge from the larger values determined from the Pb atoms. On the $SrRuO_3$ side, nevertheless, a reversed tendency

($c_{p\text{-Sr}} < c_{p\text{-Ru}}$) is observed in ~3 pseudocubic unit cells near the interface.

These divergent behaviors, reflecting a rearrangement of atomic positions inside the unit cells, can be attributed to lattice responses to polarization screening at both interfaces. For the horizontal O2-Ru-O2 atomic planes of $SrRuO_3$ [Fig. 1(c)], the in-phase octahedral rotation results in alternate up and down shifts of O2 atoms around the Ru positions. On approaching the interface, the displacements decrease in magnitude and penetrate into the PZT layer by 2 unit cells [Fig. 2(b)]. Meanwhile, the polar displacements of O2 atoms ($\delta z_{\text{O2-Zr/Ti}}$) in PZT also propagate into the $SrRuO_3$ electrode by 1–2 pseudocubic unit cells. As a result of interface bonding [13,42] and polarization screening, the antiferrodistortive order then couples with the ferroelectric order at the heterogeneous interface, which is further evidenced by the polar displacements of Ru atoms ($\delta z_{\text{Ru-Sr}}$) near the interface [inset in Fig. 2(b)]. Another interesting point worth noting is the antiparallel displacements between Zr/Ti and O2 atoms in the two longest unit cells near the CDW. This local violation of the crystallographic symmetry can be attributed to inequivalent polarization between domain I ($P_{SZ} = 84\,\mu\text{C cm}^{-2}$) and domain II ($P_{SZ} = -45\,\mu\text{C cm}^{-2}$) [Fig. 2(c)]. The P_{SZ} profile indicates that the width of the CDW is 6 unit cells, and the polarization extrapolates 1–2 pseudocubic unit cells into the $SrRuO_3$ (see Supplemental Material [30]).

More unexpected findings are revealed by the in-plane atomic displacements [Figs. 2(d) and 2(e)]. At the PZT/$SrRuO_3$ interface, polar displacements of the B-site ($\delta x_{B\text{-}A} \approx -5$ pm) and O2 ($\delta x_{\text{O2-}B} \approx -7.5$ pm) atoms clearly show that the interfacial unit cells are monoclinically distorted [43]. Calculation reveals that the in-plane polarization is $P_{SX} \approx 23.6\,\mu\text{C cm}^{-2}$ and the width of the polarized interface is ~6 unit cells [Fig. 2(f)]. Near the CDW, the Zr/Ti atoms undergo large displacements with $\delta x_{\text{Zr/Ti-Pb}} \approx -20$ pm at the wall plane. However, the relative displacements between O2 and Zr/Ti atoms are absent. Assuming that the separation takes place between positively charged Pb^{2+} cations and negatively charged $(Zr/TiO_6)^{2-}$ octahedra [44], an in-plane polarization with $P_{SX} = 17\,\mu\text{C cm}^{-2}$ is developed inside the monoclinically distorted lattices, which is supported by first-principles calculations of CDWs on $PbTiO_3$ [45].

To quantify the interfacial chemical diffusion, atomic-resolution energy-dispersive x-ray spectroscopy (EDS) was performed on the $(x = 0.9)$PZT/$SrRuO_3$ interface areas [Fig. 3(a)]. For A-site elements, the Sr atom is found to diffuse strongly into the PZT layer over one atomic layer [Figs. 3(b) and 3(c)], while for B-site elements, the Ti atom reversely diffuses into the $SrRuO_3$ electrode over one atomic layer [Figs. 3(d) and 3(e)]. The elemental profiles reveal the asymmetric chemical diffusion and the SrO-Zr/TiO_2-plane terminated interface [Fig. 3(f)]. The composition of the first interfacial unit cell is approximately $(Pb_{0.4}Sr_{0.6})(Zr_{0.1}Ti_{0.7}Ru_{0.2})O_3$ on the PZT side and $(Sr_{0.75}Pb_{0.25})(Ru_{0.5}Ti_{0.5})O_3$ on the $SrRuO_3$ side.

These results highlight that, driven by structural and chemical reconstruction, the SrO-Zr/TiO_2 terminated PZT/$SrRuO_3$ interface is characteristic of monoclinic lattice distortion and flexible polarization rotation. Specifically, the incorporation of Sr into the PZT layer [46,47] reduces the interfacial lattice

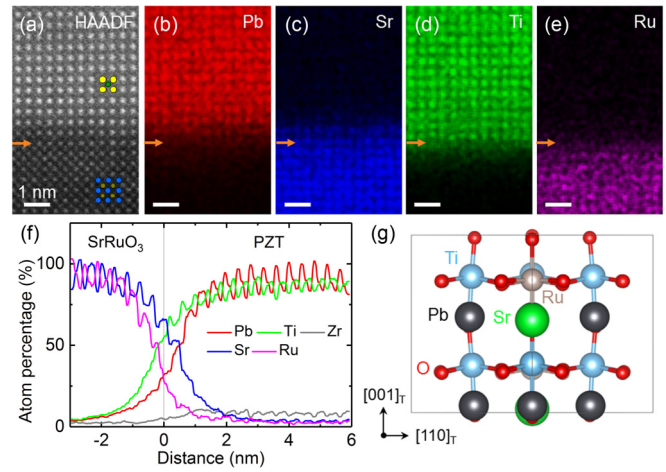

FIG. 3. (a) Atomically resolved high-angle annular dark field (HAADF)-STEM image of the $(x = 0.9)$PZT/$SrRuO_3$ interface (orange arrows) recorded along the $[100]_T$ direction. Atomic column types: Pb (yellow), Zr/Ti (green), Sr (dark yellow), Ru (blue). (b)–(e) EDS maps for Pb, Sr, Ti, and Ru, respectively. (f) Averaged atomic percentage profiles for the heavy atoms across the SrO-Zr/TiO_2 terminated interface. (g) First-principles calculated $(Pb_{0.75}Sr_{0.25})(Ti_{0.75}Ru_{0.25})O_3$ supercell (space group Cm) viewed along the $[1\bar{1}0]_T$ direction.

tetragonality and the magnitude of P_{SZ}. At the same time, a metal-to-insulator transition, which takes place at $x = 0.5$ in $Sr(Ru_{1-x}Ti_x)O_3$ [48], suppresses the interface conductivity and results in a penetration of polarization into the $SrRuO_3$ electrode. Together with the structural reconstruction, the monoclinic lattice distortion therefore facilitates the development of in-plane polarization at the interface.

This screening scenario is supported by our first-principles calculations of Sr and Ru codoped $PbTiO_3$ and a report of polarized SrO planes at $SrRuO_3/BaTiO_3$ interfaces [49]. By averaging the composition of the second-to-fourth unit cells in domain II, a supercell of $(Pb_{0.75}Sr_{0.25})(Ti_{0.75}Ru_{0.25})O_3$ was constructed for the calculation (see Supplemental Material Fig. S3 [30]). Our result shows that the supercell with monoclinic symmetry (space group Cm) has the lowest energy and the polarization is allowed to rotate freely within the confined $(1\bar{1}0)_T$ plane. By fixing the in-plane lattice constant to a bulk value of $SrRuO_3$, the out-of-plane and in-plane polarizations are $P_{SZ} = 66.2\,\mu\text{C cm}^{-2}$ and $P_{SX} = 13.2\,\mu\text{C cm}^{-2}$ for the supercell, which are close to the experimental values presented in Figs. 2(c) and 2(f). Meanwhile, the inert displacements of Ru atoms along the $[001]_T$ direction manifest their passive contribution to polarization penetration into the $SrRuO_3$ electrode [Fig. 3(g)]. Apart from the ionic screening, the decreased oxygen octahedral rotation [50,51] also provides evidence for impaired electronic screening on approaching the interface, as denoted by the yellow shadow in Fig. 2. Therefore, an *in situ* screening scenario is suggested at the oxide heterointerface [13–15].

In order to verify the validity and universality of the screening mechanism, a more complex $BiFeO_3/SrRuO_3$ interface, involving polar catastrophe, oxygen-octahedral rotation mismatch, strain mismatch, and chemical diffusion, was

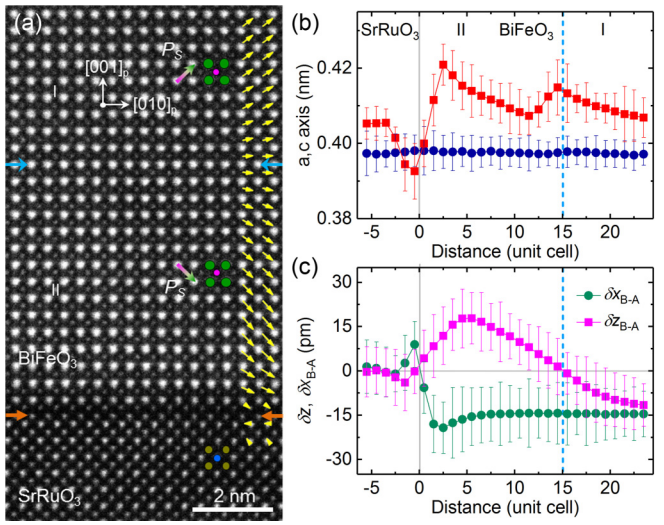

FIG. 4. (a) Atom-resolved HAADF-STEM image of the $BiFeO_3/SrRuO_3$ interface, involving polar catastrophe, oxygen-octahedral rotation mismatch ($\phi \approx 12^\circ$ for $BiFeO_3$ and $\phi \approx 6^\circ$ for $SrRuO_3$), and chemical diffusion, recorded along the $[100]_p$ direction. The yellow, orange, and blue arrows denote the polar displacement vectors compiled from (c), SrO-FeO_2 termination, and CDW, respectively. Atomic column types: Bi (green), Fe (pink), Sr (dark yellow), Ru (blue). (b), (c) Lattice parameter and polar displacement changes measured across the interface and the CDW (blue dashed lines) and plotted as a function of distance normal to the interface.

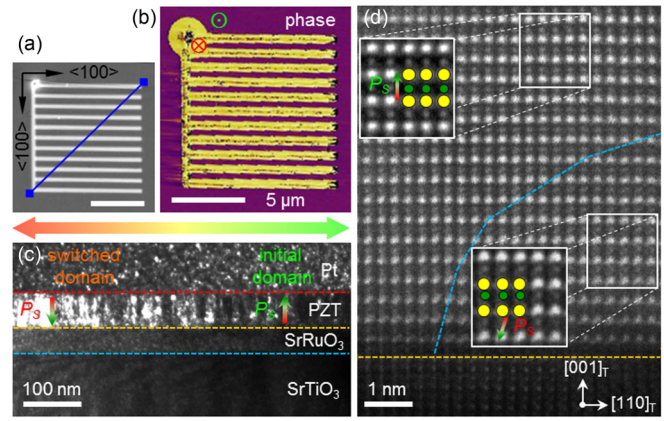

FIG. 5. *Ex situ* electric-field biasing and microscopy characterization of $x = 0.6$ PZT film. (a) Topography image of patterned Pt top electrode. The blue line denotes the location of the cross-sectional focused ion beam (FIB) lamella. (b) PFM phase image of the entire area after switching the Pt-covered regions by a +8 V voltage pulse ($\odot$ upward and $\otimes$ downward P_S orientations). (c) Dark-field TEM image of the written domain boundary recorded under two-beam conditions using $\mathbf{g} = (00\bar{2})$ reflection. The colored dashed lines mark the interfaces. (d) Corresponding atom-resolved HAADF-STEM image recorded along the $[1\bar{1}0]_T$ direction. The blue dashed line delineates the boundary between the initial and newly nucleated domains. The insets are filtered to highlight the atomic details [Pb/O1 (yellow circles), Zr/Ti (green circles)].

examined by high-angle annular dark field (HAADF)-STEM (Supplemental Material Fig. S4 [30]). In the $BiFeO_3$ layer, the lower-left-hand and upper-left-hand displacements of Fe clearly identify a tail-to-tail 71° or 109° CDW with the domain polarization pointing along the projected $\langle 011 \rangle_p$ direction [Fig. 4(a)]. Similarly, the epitaxial growth relationship yields a constant a_p axis (~0.3980 nm) and the CDW leads to lattice expansion ($c/a \approx 1.042$) with respect to the domains ($c/a \approx 1.024$) [Fig. 4(b)]. Nevertheless, the c_p axis is found to reduce abruptly from 0.4209 nm ($c/a \approx 1.057$) to 0.3926 nm ($c/a \approx 0.986$) as passing across the interface, which is accompanied with a decrease/increase in out-of-plane/in-plane displacements ($\delta z_{\text{Fe-Bi}}/\delta x_{\text{Fe-Bi}}$) on the $BiFeO_3$ side, and dominance of the in-plane displacements ($\delta z_{\text{Ru-Sr}} \approx 8.9$ pm) on the $SrRuO_3$ side [Fig. 4(c)]. These structural changes provide evidence for a monoclinlike lattice distortion at the $BiFeO_3/SrRuO_3$ interface (~6 unit cells thick) and the CDW, thereby enabling the polarization to rotate flexibly within the symmetry-permitted planes [Fig. 4(a)].

Apart from the SrO-BO_2 termination, the PZT/$SrRuO_3$ interfaces terminated by RuO_2-PbO atomic planes were also investigated (Supplemental Material Fig. S5 [30]). The impact of interface termination type on internal built-in field is discussed with respect to the measured hysteresis loops (Supplemental Material Fig. S6 [30]). In contrast to the SrO-BO_2 termination, the RuO_2-PbO termination results in a downward orientation of P_S (towards the interface) in the entire c domain. According to density-functional theory calculation [52], the worse/better screening capability of a $SrRuO_3$ electrode with SrO/RuO_2 termination may therefore explain the presence/absence of the interfacial CDWs inside the c domains [30]. More importantly, the interface reconstruction enabled flexible polarization rotation is also verified at the RuO_2-PbO terminated interfaces, independent of the change in oxygen partial pressure (0.1–1 mbar) during sample growth (Supplemental Material Fig. S7 [30]). In analogy to oxide electrodes, Au and Pt electrodes also lead to flexible polarization rotation at the metal-electrode/PZT interfaces, which are about 3 unit cells (Supplemental Material Fig. S8 [30]). The observed universality of the screening mechanism suggests that the ferroelectric-metal interfaces may act as seeds to nucleate new domains during the polarization switching process. Considering the distinct switching dynamics of ferroelastic domains [53,54], the model system Pt/($x = 0.6$)PZT/$SrRuO_3$/$SrTiO_3$, with a monodomain ferroelectric state, was selected to confirm this argument by means of *ex situ* biasing and TEM/STEM investigations (Supplemental Material Fig. S9 [30]).

By switching the Pt-electrode covered regions, an array of 180° domains, with the DWs lying in the $(100)_T$ plane, was achieved in the Pt patterned square area [Figs. 5(a) and 5(b)]. A nonuniform piezoresponse force microscopy (PFM) phase image suggests that the polarization in the targeted regions was not fully switched. Manifested by bright-contrast spots, cross-sectional dark-field TEM imaging shows that incomplete domain switching leads to preferential nucleation of nanodomains (diameter at 3–14 nm) near the PZT/$SrRuO_3$ and Pt/PZT interfaces [Fig. 5(c)]. This is confirmed by atom-resolved HAADF-STEM observations on the written DW area. The newly created nanodomains near the interfaces, which are surrounded by the initial-state domain with an upward P_S orientation, are found to possess a reversed P_S orientation along with in-plane atomic displacements [Fig. 5(d)]. This

result confirms that the low-symmetric ferroelectric-metal interfaces indeed induce the nucleation of new domains during the polarization switching process.

The seed effect of the ferroelectric-metal interface is further supported by the observation of polarization curling and flux closure structures in multiferroic $Co/PbTiO_3/(La, Sr)MnO_3$ tunnel junctions [55], in which flexible polarization rotation is identified near both interfaces. Since the in-plane polarization component does not contribute to the interface capacitance, it therefore plays a deleterious role in practical ferroelectric devices [56]. In addition, a photoemission and x-ray absorption study reveals that Ti remains tetravalent in the $Sr(Ru_{1-x}Ti_x)\,O_3 (0 \leqslant x \leqslant 1)$ films [57], suggesting that oxygen vacancies, which may be generated in the operating devices, are not a necessary ingredient for the compensation of ferroelectric polarization at the initial-state interfaces.

In fact, the screening scenario deciphered at the ferroelectric-metal heterointerfaces is analogous to the behavior at interfacial CDWs. Driven by a polarization discontinuity, monocliniclike lattice distortion associated with atomic rearrangement enables the development of in-plane polarization. As a result, flexible polarization rotation leads to a cycloidal polarization configuration at the CDWs [Figs. 1(d) and 4(c)], which is different from the reported charged 180° and 90° DWs in $PbTiO_3$ films [41,58] and charged 71°, 109°, and 180° DWs in $BiFeO_3$ films [59]. Consideration of the electrostatic energy indicates that the in-plane polarizations at the interface and the CDW are independent of each other [43], as a Néel-like DW configuration would otherwise be favored between the interfacial areas.

In summary, driven by structural and chemical mismatches, the ferroelectric-metal interfaces universally adopt low-symmetry monoclinic structures via breaking of the parent lattice symmetries [60–62]. As a consequence, the polarization screening is implemented by flexible polarization rotation at the heterogeneous interfaces, which are responsible for the nucleation of new domains during the polarization switching process. In order to overcome the degradation of the ferroelectric devices [3], our findings suggest that interface engineering, e.g., conductivity modification by inserting alien atomic monolayers [63,64], is expected to revive the screening effectiveness of the electrodes. It is hoped that such measures may overcome the long-standing fatigue issue and that applications of ferroelectric-based devices will become widespread in the future.

The research leading to these results has received funding from the European Research Council under the EU 7th Framework Programme (FP7/2007-2013)/ERC Grant Agreement No. [268058] Mobile-W and from the EU 7th Framework Programme under Grant Agreement No. 312483 - ESTEEM2 (Integrated Infrastructure Initiative–I3). Y.Y. and L.B. acknowledge ONR Grants No. N00014-12-1-1034 and No. N00014-17-1-2818. The authors thank M. Kruth and D. Meertens for sample preparation using a focused ion beam.

[1] W. Lee, H. Han, A. Lotnyk, M. A. Schubert, S. Senz, M. Alexe, D. Hesse, S. Baik, and U. Gosele, Nat. Nanotechnol. **3**, 402 (2008).
[2] Y. Cho, S. Hashimoto, N. Odagawa, K. Tanaka, and Y. Hiranaga, Nanotechnology **17**, S137 (2006).
[3] A. K. Tagantsev, I. Stolichnov, E. L. Colla, and N. Setter, J. Appl. Phys. **90**, 1387 (2001).
[4] D.-H. Do, P. G. Evans, E. D. Isaacs, D. M. Kim, C. B. Eom, and E. M. Dufresne, Nat. Mater. **3**, 365 (2004).
[5] X. Zou, L. You, W. G. Chen, H. Ding, D. Wu, T. Wu, L. Chen, and J. Wang, ACS Nano **6**, 8997 (2012).
[6] Y.-H. Hsieh, F. Xue, T. Yang, H.-J. Liu, Y. Zhu, Y.-C. Chen, Q. Zhan, C.-G. Duan, L.-Q. Chen, Q. He, and Y.-H. Chu, Nat. Commun. **7**, 13199 (2016).
[7] Y. Zhou, H. K. Chan, C. H. Lam, and F. G. Shin, J. Appl. Phys. **98**, 024111 (2005).
[8] V. Garcia and M. Bibes, Nat. Commun. **5**, 4289 (2014).
[9] J. M. Hu, L. Q. Chen, and C. W. Nan, Adv. Mater. **28**, 15 (2016).
[10] D. J. Kim, J. Y. Jo, Y. S. Kim, Y. J. Chang, J. S. Lee, J.-G. Yoon, T. K. Song, and T. W. Noh, Phys. Rev. Lett. **95**, 237602 (2005).
[11] P. Yu, W. Luo, D. Yi, J. X. Zhang, M. D. Rossell, C. H. Yang, L. You, G. Singh-Bhalla, S. Y. Yang, Q. He, Q. M. Ramasse, R. Erni, L. W. Martin, Y. H. Chu, S. T. Pantelides, S. J. Pennycook, and R. Ramesh, Proc. Natl. Acad. Sci. USA **109**, 9710 (2012).
[12] Y. J. Shin, Y. Kim, S. J. Kang, H. H. Nahm, P. Murugavel, J. R. Kim, M. R. Cho, L. Wang, S. M. Yang, J. G. Yoon, J. S. Chung, M. Kim, H. Zhou, S. H. Chang, and T. W. Noh, Adv. Mater. **29**, 1602795 (2017).
[13] N. Sai, A. M. Kolpak, and A. M. Rappe, Phys. Rev. B **72**, 020101(R) (2005).
[14] G. Gerra, A. K. Tagantsev, N. Setter, and K. Parlinski, Phys. Rev. Lett. **96**, 107603 (2006).
[15] M. Stengel, D. Vanderbilt, and N. A. Spaldin, Nat. Mater. **8**, 392 (2009).
[16] A. N. Morozovska, E. A. Eliseev, S. V. Svechnikov, A. D. Krutov, V. Y. Shur, A. Y. Borisevich, P. Maksymovych, and S. V. Kalinin, Phys. Rev. B **81**, 205308 (2010).
[17] C. S. Hwang, J. Appl. Phys. **92**, 432 (2002).
[18] D. P. Vijay and S. B. Desu, J. Electrochem. Soc. **140**, 2640 (1993).
[19] F. Chen and A. Klein, Phys. Rev. B **86**, 094105 (2012).
[20] M. F. Chisholm, W. Luo, M. P. Oxley, S. T. Pantelides, and H. N. Lee, Phys. Rev. Lett. **105**, 197602 (2010).
[21] S.-B. Mi, C.-L. Jia, I. Vrejoiu, M. Alexe, and D. Hesse, Adv. Mater. Interfaces **2**, 1500087 (2015).
[22] Y. M. Kim, A. Morozovska, E. Eliseev, M. P. Oxley, R. Mishra, S. M. Selbach, T. Grande, S. T. Pantelides, S. V. Kalinin, and A. Y. Borisevich, Nat. Mater. **13**, 1019 (2014).
[23] F. F. Krause, M. Schowalter, T. Grieb, K. Muller-Caspary, T. Mehrtens, and A. Rosenauer, Ultramicroscopy **161**, 146 (2016).
[24] Y. G. So and K. Kimoto, J. Electron Microsc. **61**, 207 (2012).
[25] C. L. Jia, M. Lentzen, and K. Urban, Science **299**, 870 (2003).
[26] K. W. Urban, C. L. Jia, L. Houben, M. Lentzen, S. B. Mi, and K. Tillmann, Philos. Trans. R. Soc., A **367**, 3735 (2009).
[27] C. L. Jia, L. Houben, A. Thust, and J. Barthel, Ultramicroscopy **110**, 500 (2010).

[28] A. T. Zayak, X. Huang, J. B. Neaton, and K. M. Rabe, Phys. Rev. B **74**, 094104 (2006).

[29] X. K. Wei, T. Sluka, B. Fraygola, L. Feigl, H. Du, L. Jin, C. L. Jia, and N. Setter, ACS Appl. Mater. Interfaces **9**, 6539 (2017).

[30] See Supplemental Material at http://link.aps.org/supplemental/10.1103/PhysRevB.98.020102 for details on experimental methods, domain configurations, surface and interface information for the ($x = 0.9,\ 0.6$) PZT and $BiFeO_3$ films, quantitative atom-resolved (S)TEM studies, identification of interface termination, first-principles calculations, effects of polar catastrophe, RuO_2-PbO termination, oxygen partial pressure, polarization orientation and strain mismatch on polarization screening, effect of interface termination on internal built-in fields, and implementation of *ex situ* biasing experiments, which includes Refs. [31–40].

[31] L. Feigl, P. Yudin, I. Stolichnov, T. Sluka, K. Shapovalov, M. Mtebwa, C. S. Sandu, X. K. Wei, A. K. Tagantsev, and N. Setter, Nat. Commun. **5**, 4677 (2014).

[32] I. Stolichnov, M. Iwanowska, E. Colla, B. Ziegler, I. Gaponenko, P. Paruch, M. Huijben, G. Rijnders, and N. Setter, Appl. Phys. Lett. **104**, 132902 (2014).

[33] W. Zhong, R. D. King-Smith, and D. Vanderbilt, Phys. Rev. Lett. **72**, 3618 (1994).

[34] P. D. Nellist and S. J. Pennycook, Adv. Imaging Electron Phys. **113**, 147 (2000).

[35] G. Kresse and J. Furthmuller, Phys. Rev. B **54**, 11169 (1996).

[36] G. Kresse and D. Joubert, Phys. Rev. B **59**, 1758 (1999).

[37] O. Grånäs, I. Di Marco, O. Eriksson, L. Nordström, and C. Etz, Phys. Rev. B **90**, 165130 (2014).

[38] S. V. Kalinin, A. Borisevich, and D. Fong, ACS Nano **6**, 10423 (2012).

[39] L. Feigl, P. E. Janolin, T. Yamada, M. Iwanowska, C. S. Sandu, and N. Setter, Appl. Phys. Lett. **106**, 032902 (2015).

[40] M. J. Highland, T. T. Fister, D. D. Fong, P. H. Fuoss, C. Thompson, J. A. Eastman, S. K. Streiffer, and G. B. Stephenson, Phys. Rev. Lett. **107**, 187602 (2011).

[41] C.-L. Jia, S.-B. Mi, K. Urban, I. Vrejoiu, M. Alexe, and D. Hesse, Nat. Mater. **7**, 57 (2007).

[42] M. G. Han, M. S. Marshall, L. Wu, M. A. Schofield, T. Aoki, R. Twesten, J. Hoffman, F. J. Walker, C. H. Ahn, and Y. Zhu, Nat. Commun. **5**, 4693 (2014).

[43] X.-K. Wei, C.-L. Jia, T. Sluka, B.-X. Wang, Z.-G. Ye, and N. Setter, Nat. Commun. **7**, 12385 (2016).

[44] N. Zhang, H. Yokota, A. M. Glazer, Z. Ren, D. A. Keen, D. S. Keeble, P. A. Thomas, and Z. G. Ye, Nat. Commun. **5**, 5231 (2014).

[45] X. Wu and D. Vanderbilt, Phys. Rev. B **73**, 020103(R) (2006).

[46] D. H. Kang, J. H. Kim, J. H. Park, and K. H. Yoon, Mater. Res. Bull. **36**, 265 (2001).

[47] T. Qi, I. Grinberg, and A. M. Rappe, Phys. Rev. B **82**, 134113 (2010).

[48] K. W. Kim, J. S. Lee, T. W. Noh, S. R. Lee, and K. Char, Phys. Rev. B **71**, 125104 (2005).

[49] P. Aguado-Puente, and J. Junquera, Phys. Rev. Lett. **100**, 177601 (2008).

[50] W. Lu, W. Song, P. Yang, J. Ding, G. M. Chow, and J. Chen, Sci. Rep. **5**, 10245 (2015).

[51] R. Gao, Y. Dong, H. Xu, H. Zhou, Y. Yuan, V. Gopalan, C. Gao, D. D. Fong, Z. Chen, Z. Luo, and L. W. Martin, ACS Appl. Mater. Interfaces **8**, 14871 (2016).

[52] S. Divilov, M.-V. Fernandez-Serra, and M. Dawber, APS March Meeting, http://meetings.aps.org/link/BAPS.2015.MAR.J13.6 (2015).

[53] P. Gao, J. Britson, J. R. Jokisaari, C. T. Nelson, S. H. Baek, Y. Wang, C. B. Eom, L. Q. Chen, and X. Pan, Nat. Commun. **4**, 2791 (2013).

[54] P. Gao, J. Britson, C. T. Nelson, J. R. Jokisaari, C. Duan, M. Trassin, S. H. Baek, H. Guo, L. Z. Li, Y. R. Wang, Y. H. Chu, A. M. Minor, C. B. Eom, R. Ramesh, L. Q. Chen, and X. Q. Pan, Nat. Commun. **5**, 3801 (2014).

[55] J. J. Peters, G. Apachitei, R. Beanland, M. Alexe, and A. M. Sanchez, Nat. Commun. **7**, 13484 (2016).

[56] M. Stengel and N. A. Spaldin, Nature (London) **443**, 679 (2006).

[57] J. Kim, J. Y. Kim, B. G. Park, and S. J. Oh, Phys. Rev. B **73**, 235109 (2006).

[58] Y. L. Tang, Y. L. Zhu, Y. J. Wang, W. Y. Wang, Y. B. Xu, W. J. Ren, Z. D. Zhang, and X. L. Ma, Sci. Rep. **4**, 4115 (2014).

[59] W.-Y. Wang, Y.-L. Tang, Y.-L. Zhu, Y.-B. Xu, Y. Liu, Y.-J. Wang, S. Jagadeesh, and X.-L. Ma, Adv. Mater. Interfaces **2**, 1500024 (2015).

[60] S. R. Spurgeon, P. V. Balachandran, D. M. Kepaptsoglou, A. R. Damodaran, J. Karthik, S. Nejati, L. Jones, H. Ambaye, V. Lauter, Q. M. Ramasse, K. K. Lau, L. W. Martin, J. M. Rondinelli, and M. L. Taheri, Nat. Commun. **6**, 6735 (2015).

[61] A. Y. Borisevich, H. J. Chang, M. Huijben, M. P. Oxley, S. Okamoto, M. K. Niranjan, J. D. Burton, E. Y. Tsymbal, Y. H. Chu, P. Yu, R. Ramesh, S. V. Kalinin, and S. J. Pennycook, Phys. Rev. Lett. **105**, 087204 (2010).

[62] C. Chen, S. Lv, J. Li, Z. Wang, X. Liang, Y. Li, D. Viehland, K. Nakajima, and Y. Ikuhara, Appl. Phys. Lett. **107**, 031601 (2015).

[63] P. Z. Wang, T. Y. Cai, S. Ju, and Y. Z. Wu, Sci. Rep. **6**, 24209 (2016).

[64] D. Stornaiuolo, C. Cantoni, G. M. De Luca, R. Di Capua, E. Di Gennaro, G. Ghiringhelli, B. Jouault, D. Marre, D. Massarotti, F. Miletto Granozio, I. Pallecchi, C. Piamonteze, S. Rusponi, F. Tafuri, and M. Salluzzo, Nat. Mater. **15**, 278 (2016).